Microscale damage evolutions in fiber-reinforced composites with different initial defects

Junjie Ye[a,b], Yun Hong[a], Lu Liu [a], Heng Cai[a], Wangpeng He[b], Bo Huang[c],
Mohamed Saafi[c], Yongkun Wang[a], Jianqiao Ye[c*]

[a]*Research Center for Applied Mechanics, Key Laboratory of Ministry of Education for Electronic Equipment Structure Design, Xidian University, Xi'an 710071, China*

[b]*Shaanxi Key Laboratory of Space Extreme Detection, Xidian University, Xi'an 710071, China*

[c]*Department of Engineering, Lancaster University, Lancaster LA1 4YW, UK*

Abstract: In this study, an effective microscale model for fiber-reinforced composites with initial damages is presented to investigate local stress distribution and damage evolution at constitutive material level. To validate the proposed numerical model, experimental data of uniaxial stress-strain responses and off-axis failure strength are employed for a comparison, and a good agreement by comparing with numerical results can be found. To represent the microscale damage evolution in the representative volume element, stiffness degradation coefficients are subtly applied to describe the failure sub-cells. Moreover, microscale damage evolutions and local stress distribution in the composites subjected to uniaxial and biaxial loads are both investigated. The effect of three different modes of initial damage in the composites are studied. The influences of the distribution, location and orientation of initial damage on damage evolutions are also studied.

Keywords: Stiffness degradation, Initial damages, Microscale damage evolution, Composites.

1. Introduction

In recent years, composites have increasingly become one of the most commonly-used structural materials. They have been used, for example, to form large airplane components such as fuselage and aerofoil, etc [1-3], due to their high strength and low density [4-6]. However, it is inevitable that voids or some initial defects are introduced in the manufacturing process of fiber reinforced composites [7-8]. These initial defects result in not only a degradation of the materials, but also further cracking when the materials are under service loads. Naturally, damage evolution causes reduction in the stiffness of composites, and has also a significant influence on their functions [9-11]. Thus, investigations on microscale damage evolutions and the effect of initial defects on a wide range of composite properties and the mechanisms leading to failure have become an attracted research topic.

Experimental tests by X-ray micro-computed tomography (micro-CT) technology have been used to detect internal voids/damages on advanced composite structures [12-13], and demonstrated that the technology is capable of evaluating damage evolutions in composites. Barbière et al. [14] studied the induced fatigue damage mechanisms of woven composites by acoustic emission and micro-CT. The related images revealed that cracks were derived from the coalescence of partial debondings at the interfaces between yarn and matrix. Cai et al. [15] effectively evaluated initial damage/void ratio and damage distribution in anisotropic polymer composites by micro-CT. According to the statistical results of fiber projection on two coordinate planes perpendicular to each other, a 3D microscale model was presented to predict their elastic modulus. Fritz et al. [16] employed micro-CT to quantify morphology in aerospace-grade fiber prepreg composites, and concentrated on exploring overall void fractions. To clearly observe the process of internal damage evolution, an in-situ micro-

Corresponding author.
E-mail: j.ye2@lancaster.ac.uk (Jianqiao Ye).

CT monitoring system may be used. Zhang et al. [17] studied the damage evolution in 3D braided composites. The research revealed that the damage modes under transverse loading were mainly attributed to interfacial debonding and matrix cracking. Cosmi and Bernasconi [18-19] studied the damage evolution in composite specimens subjected to fatigue load by means of micro-CT. Although micro-CT plays an important role in the identification of microscale damages, the test procedure with consideration of fatigue cycling or tensile condition has to be interrupted at various stages. This makes micro-CT test extremely time consuming in visualizing microscale damages with a desired resolution. For instance, a scan test executed on a specimen may require 4 hours or more [20].

As an effective supplement to the experimental method, numerical modeling shows attractive development potentials in studying void formation [21], void ratio and their influences on the mechanical properties of composites [22-23]. To study the mechanical properties of continuous fiber-reinforced composite structures, such as composite laminates, fibers are normally assumed to be periodically distributed in a matrix as shown in Fig. 1(a). Herein $\mathbf{x} = (x_1, x_2, x_3)$ and $\mathbf{y} = (y_1, y_2, y_3)$ denote global and local coordinate systems, respectively. Through discretizing the representative volume element (RVE) with a series of rectangular meshes, the finite-volume direct averaging micromechanics (FVDAM) was used with the consideration of displacement and traction continuity between adjacent sub-cells derived from a direct volume averaging technique in the fluid mechanics [24-25]. Later, the rectangular mesh is reconstructed by a parametric mapping relation (Fig. 1(b)), and the new numerical method is named as parametric FVDAM [26-28]. For the parametric element in the $y_2 - y_3$ coordinate system, it can be easily acquired by employing a linear mapping relation, which is capable of predicting macroscopic mechanical behaviors of composites with consideration of thermal residual stress [29], nonlinear deformation [30] and thermo-electro-elastic coupling [31]. Recently, the parametric FVDAM has been extended to study the effect of initial damages/voids on nonlinear behaviors and local stress distributions of continuous fiber-reinforced composites [32]. To this end, elastic modulus and Poisson's ratio of the failed sub-cells were assumed to be 0.5 MPa and 0.01, respectively. However, studies on microscale damage evolutions in composites with initial voids/damages are rarely found in the literature.

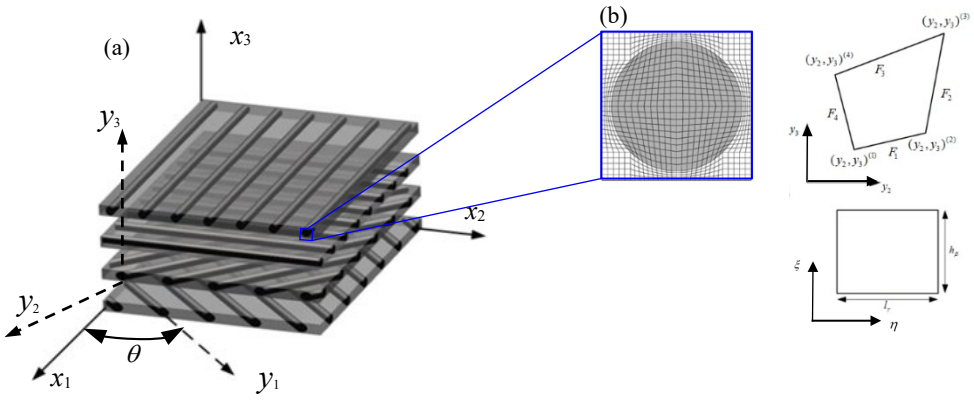

Fig. 1. The discretized procedure of the RVE (a) Composite laminates with periodically distributed fibers (b) Discretized RVE with parametric elements

Predicting stress distribution at constituent material level and understanding microscale failure mechanism are critical to estimate service life of composite structures. This study aims to explore microscale damage evolutions of composites with initial voids/damages under uniaxial and biaxial loads. To this end, the parametric FVDAM is coupled with selected failure criteria and stiffness degradation laws to study three different microscale damage modes. The outline of this study is as follows: In section 2, a microscale modeling scheme with consideration of matrix nonlinear deformations is presented. A comparison of off-axis stress-strain behaviors and failure strength of composites between numerical results and experimental data is shown in Section 3. Modeling procedure of damage evolutions with respective to initial damages is introduced in Section 4. Microscale damage evolutions under uniaxial and biaxial load are studied in Section 5. The conclusions are shown in Section 6.

2. Nonlinear modeling scheme

From the homogenization theory and sub-cell geometric equations, the sub-cell displacements $u_i'^{(q)}$ and the macroscopic average strains $\overline{\varepsilon}_{ij}$ can be expressed as follows:

$$u_i^{(q)}(\mathbf{x},\mathbf{y}(\xi,\eta)) = \overline{\varepsilon}_{ij}x_j + u_i'^{(q)}(\mathbf{y}(\xi,\eta)) \tag{1}$$

where superscript q represents the sub-cell number. $\mathbf{x}=(x_2,x_3)$ denote the global coordinate system shown in Fig. 1(a). ξ and η are the local coordinate system shown in Fig. 1(b).

For the qth sub-cell, the average stresses $\hat{\sigma}_{ij}^{(i,q)}$ on the sub-cell interfaces $F_i(i=1,2,3,4)$, as shown in Fig. 1(b), can be determined by the Hooke's law, that is,

$$\hat{\sigma}_{ij}^{(i,q)} = C_{ijkl}^{(q)}\hat{\varepsilon}_{kl}^{(i,q)} - \hat{\sigma}_{ij}^{pl(i,q)} \tag{2}$$

where $\hat{\varepsilon}_{kl}^{(i)}$ are the surface-averaged strain components on the sub-cell interface F_i. $\hat{\sigma}_{ij}^{pl(i)}$ and $C_{ijkl}^{(q)}$ are plastic stresses and sub-cell stiffness matrix, respectively. From the sub-cell equilibrium equation $\int_S \mathbf{t}^{(q)}\mathrm{d}s = \sum_{p=1}^{4} l_p\hat{\mathbf{t}}^{(p,q)} = 0$, the surface-averaged traction $\mathbf{t}^{(q)}$ and the surface-averaged displacement $\hat{\mathbf{u}}'^{(q)}$ of the qth sub-cell are given by

$$\hat{\mathbf{t}}^{(q)} = \mathbf{N}^{(q)}\mathbf{C}^{(q)}\overline{\boldsymbol{\varepsilon}} + \mathbf{K}^{(q)}\hat{\mathbf{u}}'^{(q)} + \overline{\mathbf{A}}\mathbf{N}\boldsymbol{\Phi}^{-1}\mathbf{Z}^{pl} - \mathbf{N}^{(q)}\mathbf{C}^{(q)}\hat{\boldsymbol{\sigma}}^{pl(q)} \tag{3}$$

where $\mathbf{C}^{(q)}$ and $\mathbf{K}^{(q)}$ denote sub-cell stiffness and local stiffness matrices, respectively. The matrices, $\boldsymbol{\Phi}$ and $\overline{\mathbf{A}}$, contain the dimension and the material properties of the sub-cell. $\hat{\boldsymbol{\sigma}}^{pl(q)}$ and $\mathbf{N}^{(q)}$ are the sub-cell average plastic strain and sub-cell vector, respectively. $\mathbf{Z}^{pl}$ can be obtained from the average plastic strain and co-ordinates of the sub-cell vertexes. The details of calculating the surface-averaged tractions of the qth sub-cell can be found in Pindera and Chen [28, 33].

The surface-averaged tractions and displacements between the adjacent sub-cells must satisfy the continuity conditions. With the consideration of periodic boundary conditions, the global stiffness can be written as,

$$\mathbf{K}^{global}\hat{\mathbf{U}}' = \Delta\mathbf{C}\overline{\boldsymbol{\varepsilon}} + \mathbf{G} \tag{4}$$

where $\mathbf{K}^{global}$ and $\hat{\mathbf{U}}'$ are the global stiffness matrix and unknown surface-average displacement vector, respectively. $\Delta\mathbf{C}$ is the change in stiffness between adjacent sub-cells. $\mathbf{G}$ is a force vector related to plastic deformation.

The sub-cell average strains, $\overline{\boldsymbol{\varepsilon}}^{(q)}$, can be determined by solving Eq. (4), and the sub-cell average stresses will be obtained. The relationship between the sub-cell average strains and the macroscopic strains is

$$\overline{\boldsymbol{\varepsilon}}^{(q)} = \mathbf{A}^{(q)}\overline{\boldsymbol{\varepsilon}} + \mathbf{D}^{(q)} \tag{5}$$

where $\mathbf{A}^{(q)}$ and $\mathbf{D}^{(q)}$ are sub-cell strain concentration matrix and sub-cell plastic deformation vector, respectively.

Considering the sub-cell average plastic stresses, the sub-cell average stresses $\overline{\boldsymbol{\sigma}}^{(q)}$ can be expressed as the function of sub-cell average strains in the following form:

$$\overline{\boldsymbol{\sigma}}^{(q)} = \mathbf{C}^{(q)}\overline{\boldsymbol{\varepsilon}}^{(q)} - \overline{\boldsymbol{\sigma}}^{pl(q)} \tag{6}$$

Substituting Eq. (5) into Eq. (6), the sub-cell average stresses $\overline{\boldsymbol{\sigma}}^{(q)}$ is given as

$$\overline{\boldsymbol{\sigma}}^{(q)} = \mathbf{C}^{(q)}\mathbf{A}^{(q)}\overline{\boldsymbol{\varepsilon}} + \mathbf{C}^{(q)}\mathbf{D}^{(q)} - \overline{\boldsymbol{\sigma}}^{pl(q)} \tag{7}$$

To compute the macroscopic average stress $\overline{\boldsymbol{\sigma}}$, the sub-cell average stress $\overline{\boldsymbol{\sigma}}^{(q)}$ in Eq. (7) is averaged over the entire RVE, that is,

$$\overline{\boldsymbol{\sigma}} = \mathbf{C}^{*}\overline{\boldsymbol{\varepsilon}} - \overline{\boldsymbol{\sigma}}^{pl} \tag{8}$$

where the equivalent elastic stiffness matrix $\mathbf{C}^{*}$ and the macroscopic average plastic stress $\overline{\boldsymbol{\sigma}}^{pl}$ can be obtained by the homogenization theory, that is,

$$\mathbf{C}^{*} = \sum_{q=1}^{N_q} v^{(q)}\mathbf{C}^{(q)}\mathbf{A}^{(q)} \tag{9}$$

$$\overline{\boldsymbol{\sigma}}^{pl} = \sum_{q=1}^{N_q} v^{(q)}\left(\overline{\boldsymbol{\sigma}}^{pl(q)} - \mathbf{C}^{(q)}\mathbf{D}^{(q)}\right) \tag{10}$$

where $v^{(q)} = V^{(q)}/V$, denotes the volume ratio of the qth sub-cell. $V^{(q)}$ and V are the volumes of the sub-cell and RVE, respectively.

Due to the large difference between the elastic moduli of the constituent materials, fibers are normally considered linear elastic before matrix failure occurs. The improved Bonder-Partom model, one of the commonly-used viscoplastic constitutive models, has been proved to be effectiveness in describing nonlinear deformations of polymer matrix materials [34-35]. In determining the inelastic deformation, the total strain rate $\dot{\boldsymbol{\varepsilon}}$ is assumed to be a sum of elastic strain rate $\dot{\boldsymbol{\varepsilon}}^{e}$ and inelastic strain rate $\dot{\boldsymbol{\varepsilon}}^{pl}$. The vector $\dot{\boldsymbol{\varepsilon}}^{pl}$ is written as a function of the deviatoric stress tensors s_{ij}, the effective stress σ_e, and the second-order invariant of the deviatoric stress tensor J_2, in the following form:

$$\dot{\varepsilon}_{ij}^{pl} = 2D_0 \exp\left[-\frac{1}{2}\left(\frac{Z}{\sigma_e}\right)^{2n}\right]\left(\frac{s_{ij}}{2\sqrt{J_2}} + \alpha\delta_{ij}\right) \tag{11}$$

where D_0 and n represent the maximum inelastic strain rate and sensitivity control parameter related to inelastic strain rate, respectively. The parameters Z and α, are internal state variables.

3. Off-axis failure strength of continuous fiber-reinforced composites

3.1. Failure criterion

When microscale damage evolution in composites is considered, an effective failure criterion is critical to estimate the sub-cell performance. The failure criteria can be classified into two main categories: the mode-independent failure criteria (Maximum stress, Maximum strain, Tsai-Wu, etc.) and mode-dependent failure criteria (Chang, Puck, etc.) [36-37]. Hashin criterion, one of the mode-dependent failure criteria, shows an excellent performance in predicting multiple damage modes (fiber breakages or matrix cracks). The specific descriptions of the two-dimensional Hashin failure criterion [38] in determining sub-cell failures are as follows:

When tension is in the fiber direction ($\sigma_{11} > 0$), tensile failure occurs in fibers, as defined by the following equation.

$$\left(\frac{\sigma_{11}}{X_T}\right)^2 + \beta\left(\frac{\sigma_{12}^2 + \sigma_{13}^2}{S_{12}^2}\right) = 1 \tag{12}$$

where X_T and S_{12} denote longitudinal tensile and axial shear strengths, respectively. σ_{12} and σ_{13} are longitudinal shear stresses. β is a coefficient, which determines the contribution of shear stress to longitudinal fiber failure.

When compression is in the fiber direction ($\sigma_{11} < 0$), fiber collapse failure occurs. The relation between the longitudinal compressive strength X_C and the compressive stress σ_{11} is given by

$$\left(\frac{\sigma_{11}}{X_C}\right)^2 = 1 \tag{13}$$

If the tension is in the direction perpendicular to the fiber direction ($\sigma_{22}+\sigma_{33} > 0$), the tensile failure mainly occurs in the matrix materials. The failure criterion is as follows:

$$\left(\frac{\sigma_{22} + \sigma_{33}}{S_{22}^2}\right)^2 + \frac{1}{S_{23}^2}\left(\sigma_{23}^2 - \sigma_{22}\sigma_{33}\right) + \frac{1}{S_{12}^2}\left(\sigma_{12}^2 + \sigma_{13}^2\right) = 1 \tag{14}$$

where S_{22}, S_{23}, S_{12} are transverse tensile, transverse shear and axial shear strengths, respectively. In addition, σ_{22} and σ_{33} denote transverse stresses along y_2-direction and y_3-direction, respectively. σ_{23} is the corresponding shear stress component.

If the compression is perpendicular to the fiber direction ($\sigma_{22}+\sigma_{33} < 0$), crush failure mainly occurs in matrix. The matrix failures can be determined by

$$\left(\frac{\sigma_{22} + \sigma_{33}}{2S_{23}}\right)^2 + \left[\left(\frac{Y_c}{2S_{23}}\right)^2 - 1\right]\frac{\sigma_{22} + \sigma_{33}}{Y_c} + \frac{1}{S_{23}^2}\left(\sigma_{23}^2 - \sigma_{22}\sigma_{33}\right) + \frac{1}{S_{12}^2}\left(\sigma_{12}^2 + \sigma_{13}^2\right) = 1 \tag{15}$$

where Y_c is the transverse compressive strength.

3.2. Model validation

To validate the model, constituent material properties of the carbon fiber-reinforced epoxy matrix (CFREM) composites are shown in Table 1 [39]. The fiber volume fraction of the composite is 56%. To describe the inelastic deformation, the improved Bodner-Partom constitutive model is introduced and the viscoplastic parameters are presented in Table 2 [40]. The fiber tensile and compressive strengths are 2656MPa and 1558MPa, respectively. The matrix tensile, compressive and shear strengths are 56MPa, 250MPa and 50MPa, respectively.

Table 1. Material properties of composite materials

Materials	E_{11}/GPa	E_{22}/GPa	G_{12}/GPa	v_{12}	v_{23}
Carbon-Fiber	230	20	20	0.26	0.40
Epoxy	3.45	3.45	1.28	0.35	0.35

Table 2. Viscoplastic parameters of each component material

Materials	D_0/s	n	Z_0/MPa	Z_1/MPa	α_0	α_1	q
Carbon-Fiber	0.0	-	-	-	-	-	-
Epoxy	1×10^6	0.63	391	803	0.04	0.11	280

It should be noted that the microscale model is developed in the coordinate system $y_2 - y_3$ (see Fig. 1(a)), while the load is applied in the x_1-direction. Thus the following off-axis stress-strain relation is used,

$$\boldsymbol{\sigma}_\theta = \mathbf{T}^{-1}\mathbf{C}^*\left(\mathbf{T}^{-1}\right)^T\boldsymbol{\varepsilon}_\theta \tag{16}$$

where θ is the fiber off-axis angle. $\boldsymbol{\sigma}_\theta$ and $\boldsymbol{\varepsilon}_\theta$ are the off-axis stress and strain components, respectively. $\mathbf{C}^*$ is the effective stiffness matrix. $\mathbf{T}^{-1}$ is a 6×6 transformation matrix, the details of which can be found in the Appendix.

Fig. 2 shows the nonlinear stress-strain responses of the CFREM composite, where, the experimental results from [40] are also shown for comparisons. The test results were obtained by applying quasi-static tensile strain (strain rate 10^{-5}) on the specimens. For each loading condition, three identical specimens were tested, and the test results shown in Fig.1 are the average. In general, the numerical results have a very good agreement with the experimental data. In addition, the capability of the proposed method in predicting strength is also verified by comparing with the strength from the off-axis tensile tests in Table 3. The maximum relative error is 4.82% when fiber off-axis angle is 30°.

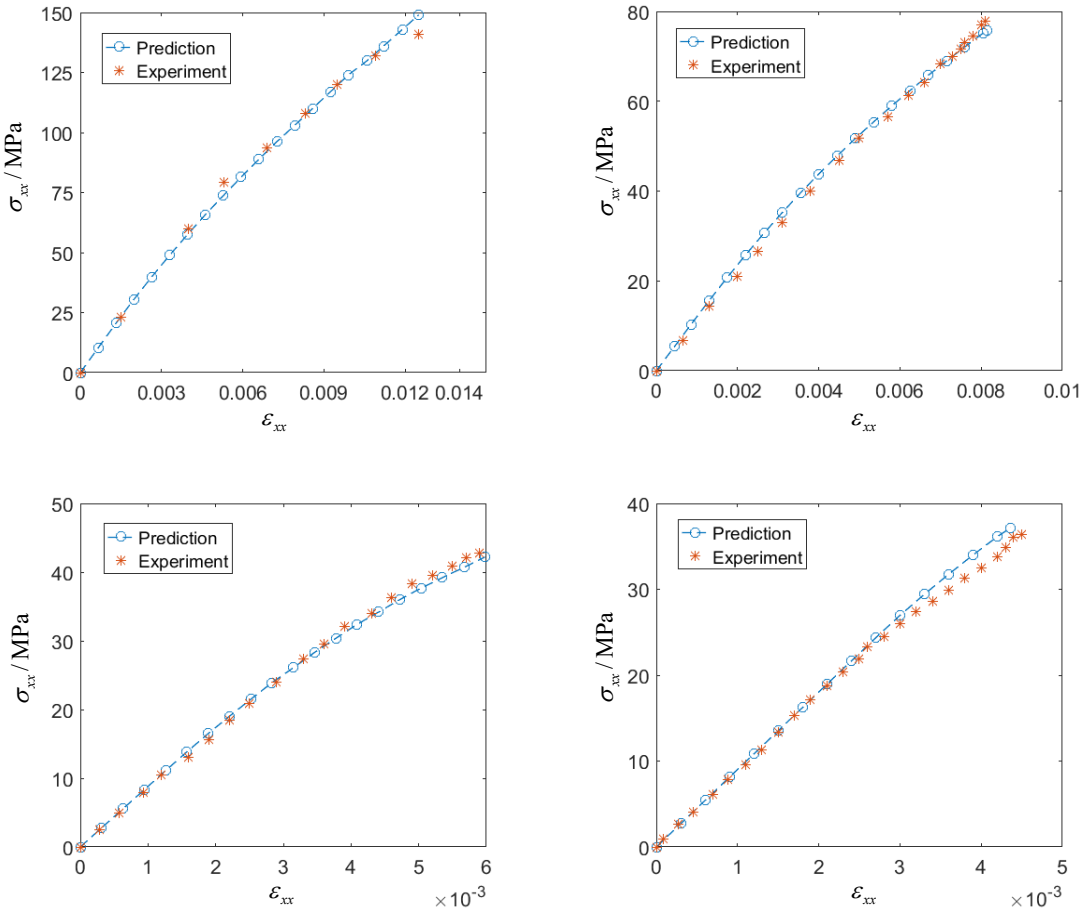

Fig. 2. Stress-strain curves of the CFREM composites with respective to four off-axis angles

Table 3. Comparison of tensile strength between numerical results and experimental data

Off-axis angle	Experiment /MPa	Prediction/MPa	Relative error
30°	141	147.80	4.82%
45°	77	77.87	1.13%
60°	43	42.74	-0.60%
90°	38	38.41	1.10%

4. Modeling procedure of damage evolutions with respective to initial damages

4.1. Microscale initial damages

Composites have microscale initial defects/voids originated from manufactural process and thermal residual stresses. It is difficult for researchers to observe internal damage evolution by experimental methods. In order to qualitatively study the influence of initial defects on damage evolution, three preset damage patterns, as shown in Fig. 3, are considered. The initial damages are embedded only in matrix due to its lower failure strength. Herein initial damage “A” is placed at the same location in the three RVEs, while initial damages “B” and “D” are placed at different locations to assess the interactions between the defects and study damage evolution. The white and gray sub-

cells denote matrix and fibers, respectively. The initial defects/voids are marked with red color.

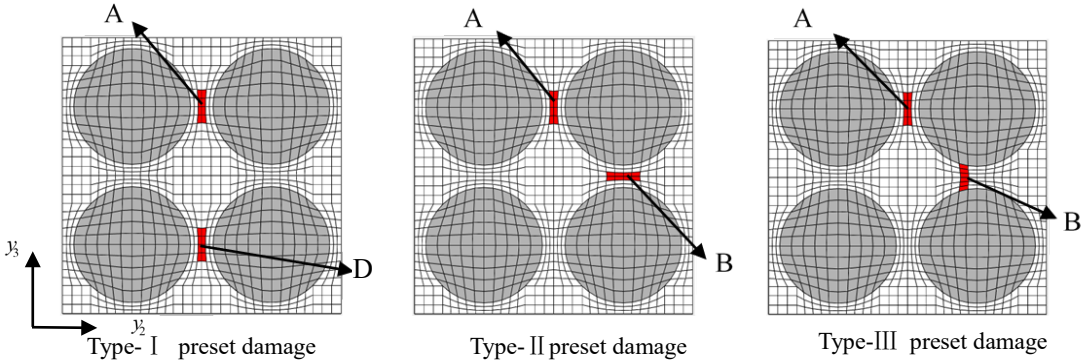

Fig. 3. Three types of preset damages

4.2. Modeling scheme of damage evolution

Sub-cell stiffness degeneration in composites occurs once local stress or strain reaches to the failure strength of constituent materials. To effectively describe damage evolutions in composites, a failure criterion has to be properly integrated with a stiffness degradation model. At present, stiffness degradation models, including the models proposed by Gotsis [41], Mayes [42], Huang [43] and McCartney [44], have been developed to be suitable for describing the stiffness degradation of polymer-matrix composites.

For the failure modes of polymer-matrix composites under tensile or compressive load, Huang and Mayes models are accurate in predicting the failure and damage of constituent materials. The degradation coefficients of the constituent materials under different load condition are shown in Table 4, where the symbol "-" denotes that the elastic moduli or/and Poisson's ratio keep constant, independent of sub-cell failure. In the process of simulating damage evolution, the elastic constants of a sub-cell are degraded by multiplying them with the degradation coefficients once the stress or strain has reached the strength of the constituents.

Table 4. Stiffness degradation coefficients under different failure modes

Failure model	E_{11}	E_{22}	E_{33}	G_{23}	G_{12}	G_{13}	v_{23}	v_{12}	v_{13}
Fiber tensile failure	0.01	-	-	-	0.01	0.01	-	0.01	0.01
Fiber compression failure	0.2	-	-	0.01	0.01	0.01	-	0.01	0.01
Matrix tensile failure	-	0.01	-	0.01	0.01	-	-	0.01	-
Matrix compression failure	-	0.2	-	0.2	0.2	-	-	0.2	-

The investigation on damage evolution has three main steps: 1) Solving the microscopic stress distributions in the RVE. 2) Analyzing the sub-cell failure, and 3) Evaluating Fiber/matrix stiffness degradation. The detailed procedures are as follows:

1) A RVE with initial damages is firstly determined and further divided into a series of sub-cells.

According to the coordinates of the sub-cell vertex, as well as the continuity relations of traction and displacement components between adjacent sub-cells, a parametric FVDAM model is established.

2) Initial sub-cell strains and stresses are imposed as inputs, and a maximal macroscopic strain $\varepsilon_{\max}$ is preset.

3) From the numerical results of sub-cell stresses or strains derived from the nth iteration step, the Bodner-Partom constitutive model is employed simultaneously to obtain plastic deformation of the matrix and used as the inputs in the $(n+1)$th iteration.

4) The parametric FVDAM model is employed to calculate microscopic stress distributions under the macroscopic strain ε_{n+1}.

5) The failure criterion is introduced to evaluate whether any sub-cell failure has occurred. If sub-cell failure has occurred, the effective elastic constants of the failed sub-cells are reduced by multiplying them with the respective degradation coefficients.

6) A full analysis of the RVE with failed sub-cells is performed to study microscale damage evolution and failure strength of the material.

A computer program in Fortran was written to study damage evolution. To ensure the program work as intended, issues such as matrix singularity, data overflow, etc., may be avoided by implementing the followings:

1) Due to the huge difference of load-carrying capacity between fiber and matrix materials, a large load increment may result in divergence of the numerical results. A suitable strain step should be firstly determined priori to balance calculation efficiency and computation accuracy.

2) To simulate the effects of initial damages/voids on microscale damage evolution in composites, some initial damages are firstly set in the RVE. To avoid singularity of the global stiffness matrix $\mathbf{K}^{\text{global}}$ in the parametric FVDAM, the elastic constants of the initially damaged sub-cells are determined by multiplying the original elastic constants with the respective stiffness degradation coefficient.

5. Microscale analysis with respective to initial damages

5.1. Uniaxial failure analysis

To discuss the effect of initial damage/void modes (Fig. 3) on the microscale damage evolution and stiffness of the CFREM composites, uniaxial transverse tensile and compressive loads along the y_2-direction are applied on the RVE, respectively.

5.1.1. Failure strength

Fig. 4 shows the transverse stress-strain relation for the three modes of initial damage shown in

Fig. 3. For comparisons, composites without initial damage is also considered. As expected, the present of damages tends to decrease the stiffness and the failure strength of the material. In details, Type-I damage causes the greatest reduction in transverse tensile strength and stiffness. The other damage modes show the similar stress-strain relations. In other words, the reductions in stiffness caused by Type-II and Type-III initial damages are approximately the same. However, an obvious distinguish in transverse tensile strength can be found by damage modes. The predicted transverse tensile strength of the composite with Type-II and Type-III damages are 36.4MPa. 37.1MPa, respectively.

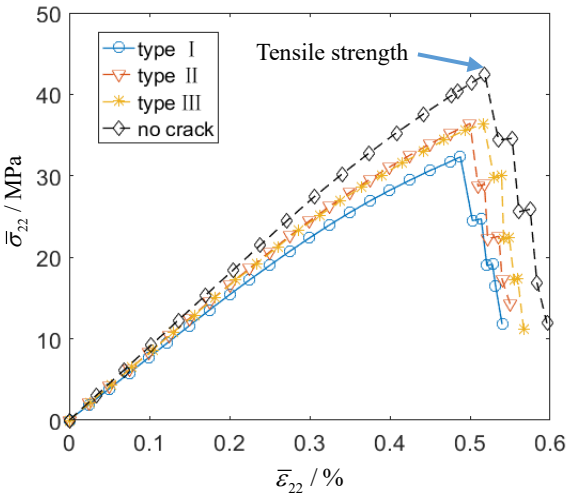

Fig. 4. Transverse tensile properties of CFREM composites with respect to the three microscale preset cracks

5.1.2. Microscale damage evolution

1) Uniaxial tension

Fig. 5 shows the transverse stress distributions and microscale damage evolution of the composites with Type-I preset damage (Fig. 3(a)) under uniaxial tensile strain. Fig. 5(a) and Fig.5 (d), respectively, show the local stress field and the damage extension when the total transverse strain is 0.476%. It shows that the maximum transverse tensile stress occurs in the vicinity of the tips of the initial damage, as shown in Fig. 5(a), and the damage propagation is perpendicular to the load direction. Fig. 5(b) and Fig. 5(e) show, respectively, the stress contour and the damage progression of the composites when the tensile strain is 0.497%. When the strain is increased to 0.518%, the stress contour and damage of the composite are shown in Fig.5 (e) and Fig. 5(f), respectively. It can be seen from Figs. 5(d)-(f) that the damage path is always perpendicular to the load direction until the preset cracks are connected, resulting in the ultimate failure of the whole RVE. In addition, it is interesting to mention from Figs. 5(a)-(c) that lower stress amplitude will be found with a further increasing of uniaxial tensile strain. This attributes to the damage extension in

the RVE, resulting in the stress unloading around the damage tips.

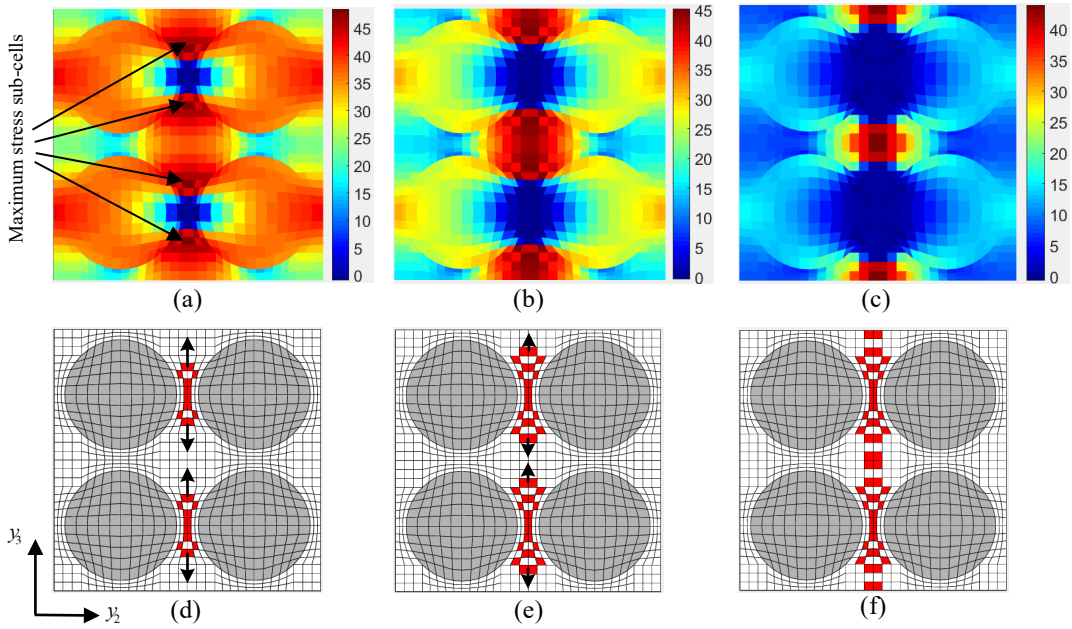

Fig. 5. Stress distribution and damage evolution of Type-I preset damage under tensile strain in the y_2-direction

Fig. 6 presents the transverse stress distribution and damage extension of the composites with Type-II preset damage (Fig. 3(b)) under uniaxial tensile strain. The figures show again that the maximum transverse stresses are located at the crack tips, and maximum transverse stress amplitude tends to slightly decrease with further damage propagation. It is noted, as shown in Fig. 6(d), that crack "A" extends perpendicular to the load direction, and some new failed sub-cells located at "C", "D" and "E" occurs. With a further increase of the transverse load, as shown in Fig. 6(f), the damages located at "A", "C", "D" and "E" extend along the y_3-direction. Moreover, the final failure is attributed to the damage coalescence between "A" and "D". In addition, it is worth noting that new sub-cell failure is hardly found around the initial damage "B" as shown in Figs. 6(d)-(f). This is due to the fact that the applied tensile strain is parallel to the surface of damage B, causing little stress concentration. However, as shown in Fig. 6(a)-(c), significant stress concentration occurs around the initial damage A whose damage surface is perpendicular to the applied tensile strain.

Fig. 7 shows the stress distribution and damage evolution due to Type-III preset damage when the RVE is subjected to uniaxial tensile strain, and the two initial damage "A" and "B" (Fig. 3(c)) are both perpendicular to the external load. Once the external transverse load is applied on the RVE, damage evolution occurs first at the tip of initial damage "A", as shown in Fig. 7(a). Similar to the effect of Type-II initial damage, new cracks occur at the same locations, i.e., "C", "D" and "E", as shown in Fig. 7(d). With a further increase of the external load, the damages located at "A" and "D" propagate along the interface between fiber and matrix, and are finally connected at "B", as shown in Figs. 7(e)-(f). The final failure is attributed to the coalescence between the new damage "D" and

the initial damages “A” and “B”. There is no new sub-cell damage found near the regions of “C” and “E” even when the whole RVE fails.

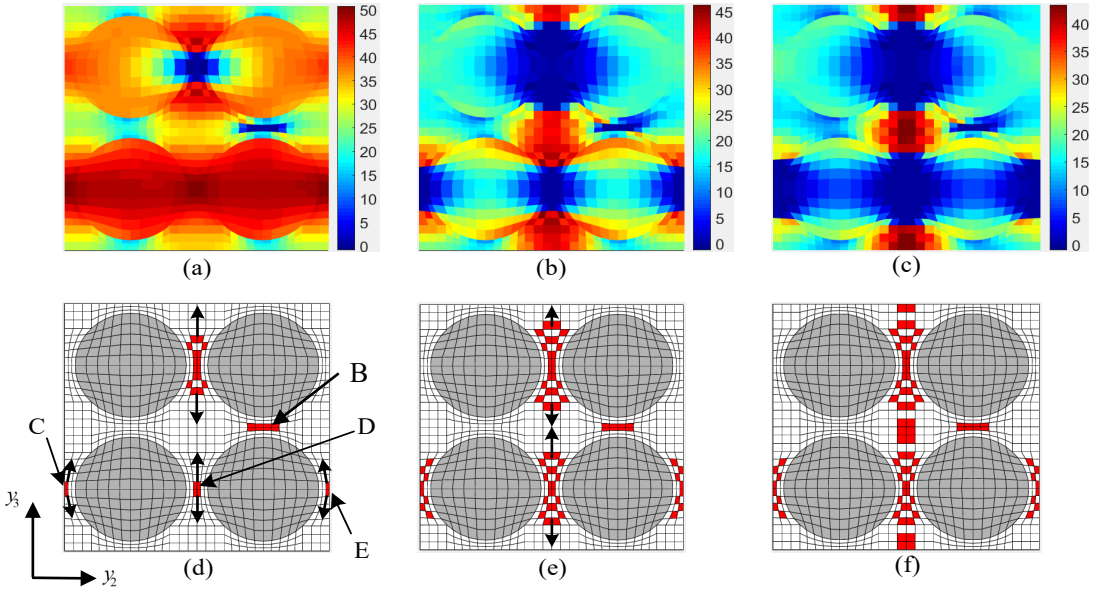

Fig. 6. Stress distribution and damage evolution of Type-II preset damage under y_2-direction tensile strain

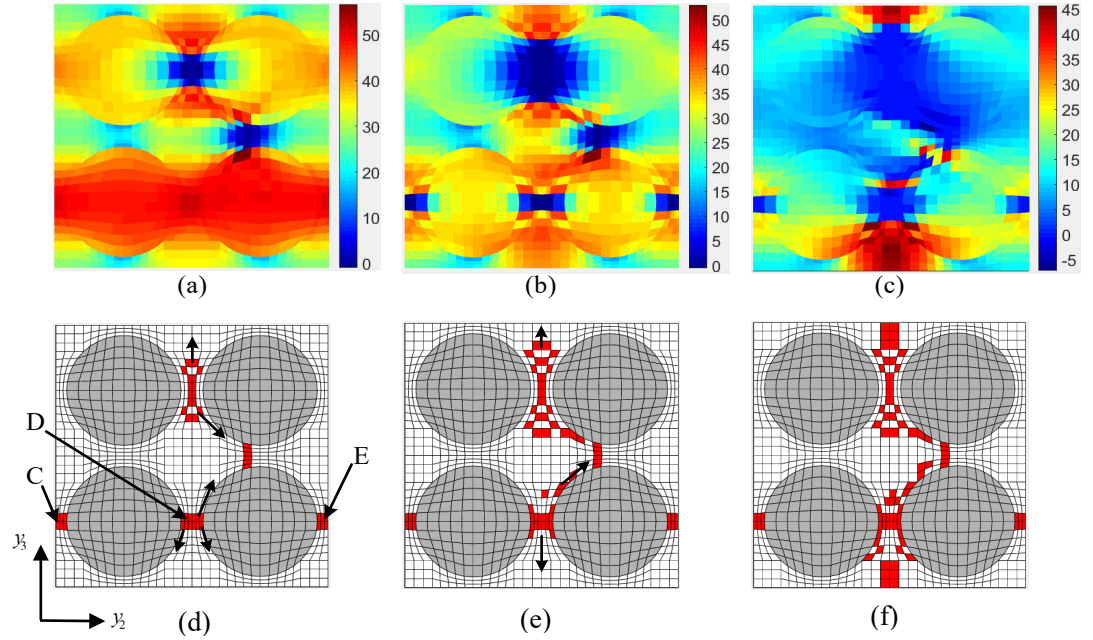

Fig. 7. Stress distribution and damage evolution of type- III preset damage under y_2-direction tensile strain

2) Uniaxial compressive analysis

To investigate compressive failure of the composites with initial damage, a transverse compressive load in the y_2-direction is applied on the RVE. Similarly, the three preset damages, as shown in Fig. 3, are considered in the example, and the stress-strain curves are shown in Fig. 8. In comparison to the tensile performance (Fig. 4), it can be seen that the CFREM composites, with and without initial damage, both show better performances, due to the higher compressive strength of the constituent materials. It also shows that the Type-I initial damage significantly reduces the stiffness and the transverse compressive strength of the material. The composites with the Type-II

damage has a higher failure strength than that with the Type-III damage. Once the sub-cell fails, the RVE fails almost immediately.

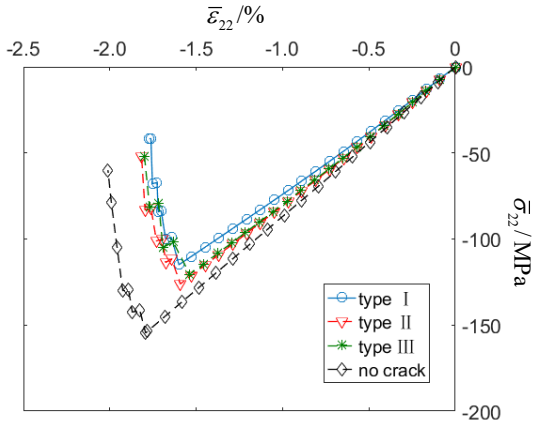

Fig. 8. Transverse compression of the CFREM composites with respective to three microscale preset damages

Fig. 9 shows the microscale properties of the composites with respective to Type-I preset damage under compressive strain in the y_2-direction . From Fig. 9(a) and Fig. 9(d), it is found that the RVE is subjected to a combination of compressive and shear stresses. The maximum transverse compressive stress σ_{22} and the maximum shear stress σ_{23} are, respectively, occur in the matrix and the fiber. Once the sub-cell stress reaches the compressive strength, the corresponding sub-cell fails. The damage propagation is perpendicular to the load direction, and limited in the matrix material (Fig. 9(g)) due to the huge differences of shear and compressive strengths between the fiber and the matrix. As shown in Figs. 9(b)-(c), a further increase of the compressive strain, the maximum compressive stress σ_{22} stays within the matrix, while the maximum shear stress σ_{23} is shifted from the fiber to the matrix (Fig. 9(f)). From Figs. 9(g)-(i), it can be seen that the sub-cell damages always extend perpendicular to the external loading direction, and the final compressive failure in the composites is attributed to the damage coalescence between "A" and "D".

The same compressive strain in y_2-direction is applied on the RVE with Type-II preset damage, and the numerical results are shown in Fig. 10. From Figs. 10(a)-(b), the maximum compressive stress σ_{22} firstly located at the tip of damage "A", and then shifted to damage location "D". With a further increase of compressive strain as shown in Fig. 10(c), an abrupt drop of stresses around damage "A" can be found. This attributes to the final failure of the RVE, resulting in the stress unloading around the damage "A". A similar conclusion can be drawn from shear stress, σ_{23}, distributions shown in Figs. 10(d)-(f). The maximum shear stress σ_{23} occurs first near "A" and then moves the vicinity of "D".

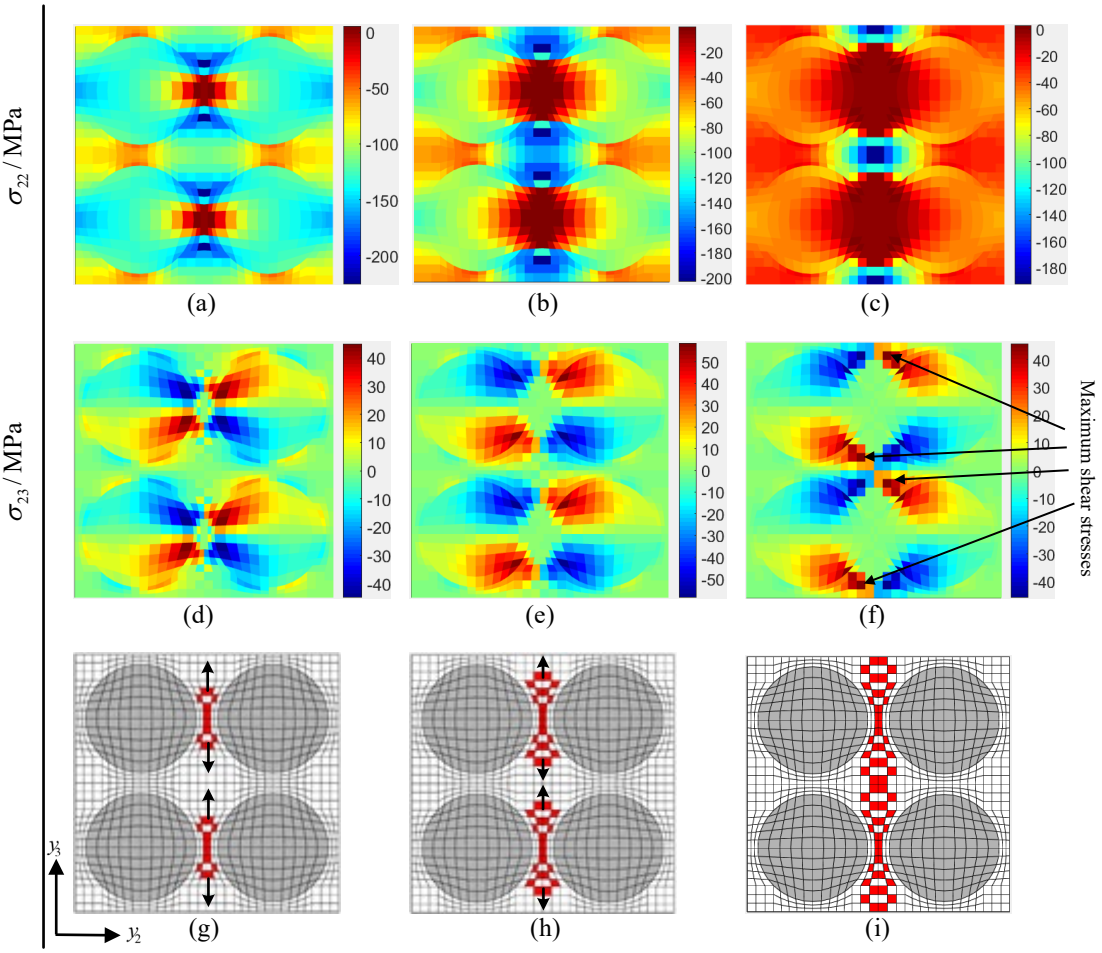

Fig. 9. Normal and shear stress distributions, as well as damage evolutions of Type-I preset damage under compressive strain in the y_2-direction

Fig. 10(g) shows that local compressive failure firstly occur at the tip of damage "A", and then extend perpendicular to the external load as shown in Fig. 10(h). Subsequently, new sub-cell failures occur around "C", "D" "E" in the RVE. The direction of damage growths at locations "A", "B" and "D" are indicated by the black arrows in Fig. 10(h). The final failure of the RVE is the result of damage coalescence between "A" and "B" as shown in Fig. 10(i). It is also found that damage location "D" grows along the tangent to the fiber-matrix interface. It is interesting to see that the new damage near "C" and "E" is no longer propagate until the RVE failures. This can be understood from the microscale stresses variation in the RVE shown in Figs. 10(a)-(f). Although the maximum compressive stress around the new damage "C" and "E" is as high as that around 'A' (Fig. 10b), the shear stress at damage "C" and "E" is significantly lower than that around 'A' as the locations are close to the shear stress free boundary, which leads to further progressive failure around 'A' until the total failure of the RVE.

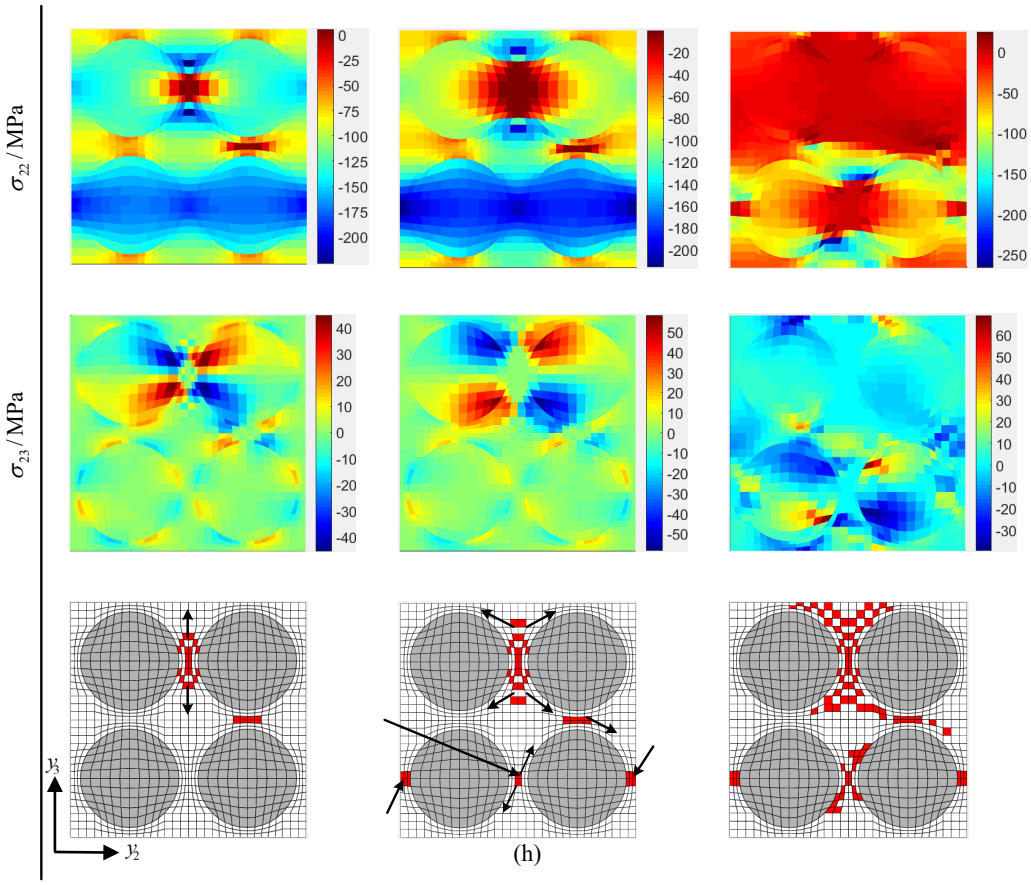

Fig. 10. Normal, shear stress distributions, and damage evolutions of Type- II preset damage under compressive strain in the y_2-direction

Fig. 11 presents the normal and the shear stress distributions, as well as microscale damage evolution for the composite with Type-III preset damage under uniaxial compression in the y_2-direction . For the distribution of σ_{22}, as shown in Figs. 11(a)-(c), the maximum compressive stress occurs first at the tip of damage "A" (Fig. 11(a)). Damage evolution shows apparent shifting of the maximum normal stress from the matrix to the fiber sub-cells as shown in Fig. 11(c). From Figs. 11(d)-(f), it can be concluded that the maximum shear stress σ_{23} always occurs in the fibers. In the early stage, some new damages concurrently occur around initial damages "A" and "B" (Fig. 11(g)), and then propagate along the tangential direction of fibers, as shown in Figs. 11(h), as the increase of compressive strain. Moreover, some new damages in the matrix materials marked red round "D" are easily seen. The final failures of the RVE is attributed to the damage coalescence between initial damages "A", "B" (Fig. 3) and new damage location "D" as shown in Fig. 11(i). It should be noted that the sub-cell failures always occur in the matrix near an interface.

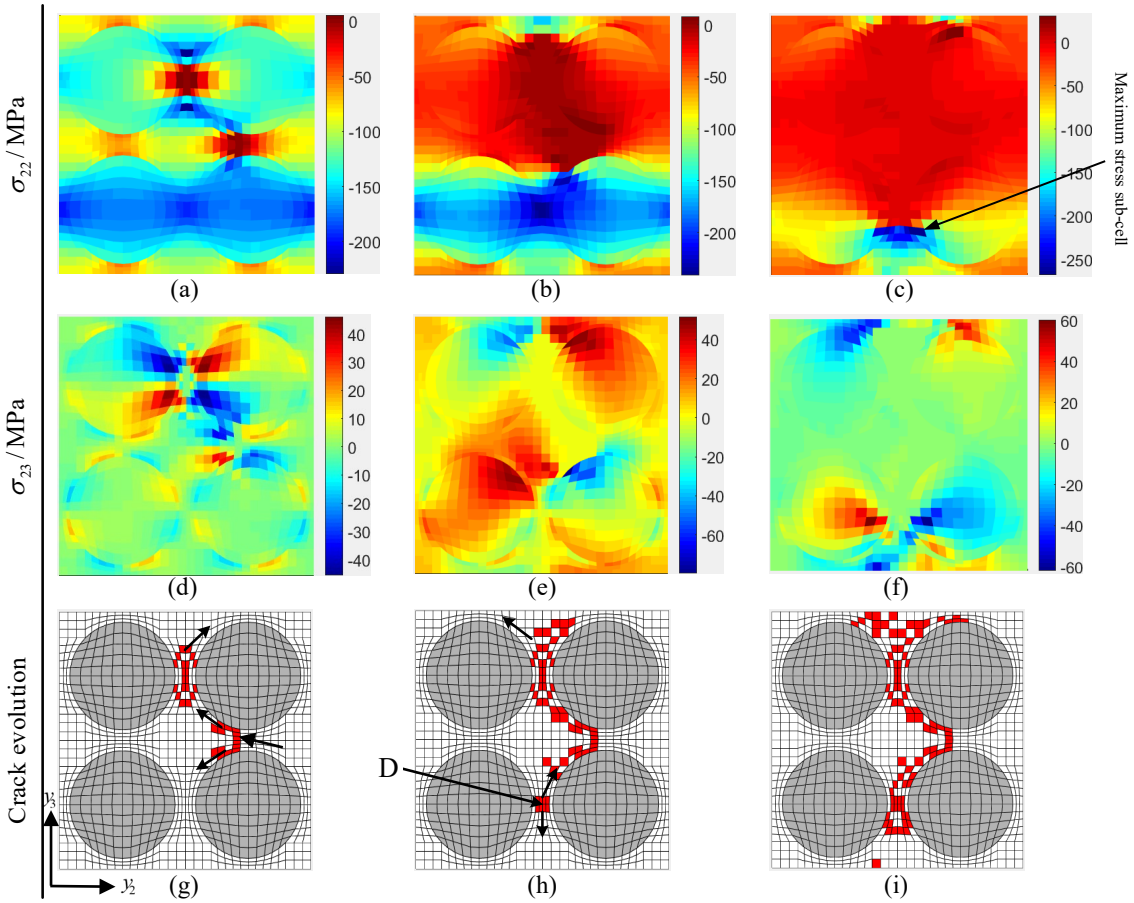

Fig. 11. Normal and shear stress distributions, as well as damage evolutions of Type-Ⅲ preset damage under y_2-direction compression load

5.2. Biaxial tensile analysis

To investigate biaxial failure of the composites, transverse strains of same magnitude ($\varepsilon_{22}=\varepsilon_{33}$) are applied simultaneously on the RVE with initial damages. Fig. 12 presents the stress-strain behaviors of the composite with Type-I initial damage. It can be seen that the stiffness in the y_2-direction is significantly lower than that in the y_3-direction. In addition, the maximum stress in the two directions are, respectively, 35.1 MPa and 41.1 MPa before new sub-cell damage occurs in the RVE.

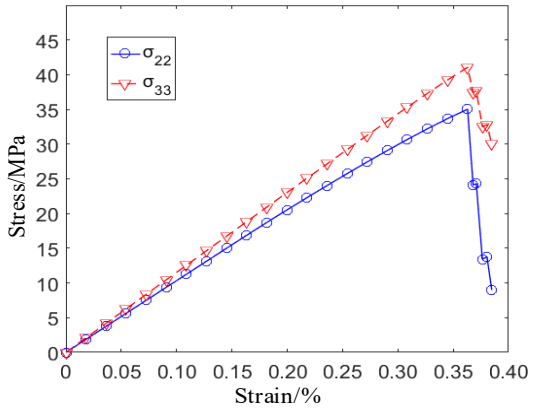

Fig. 12. Stress-strain curves of Type-I initial damage under biaxial tensile strain

The stress contour plot and damage evolution of the Type-I initial damage under biaxial transverse load are shown in Fig. 13. The transverse stress distributions of σ_{22} and σ_{33} are shown in Figs. 13(a)-(f). From Figs. 13(a)-(c), it can be seen that the maximum normal stresses σ_{22} always occur around the damaged region in the matrix. However, the maximum transverse stress σ_{33} shifts from fiber to matrix due to the damage propagation. Similar to uniaxial tension (Fig. 5), new damages occur first along the y_3-direction , and the final failure presents coalescence of the initial damages, "A" and "D", as shown in Figs. 13(g)-(i) in the matrix materials. Meanwhile, new damages, "G", "H", "I", "F", "J" and "B", appear when the final failure occurs in the RVE, as shown in Fig. 13(i).

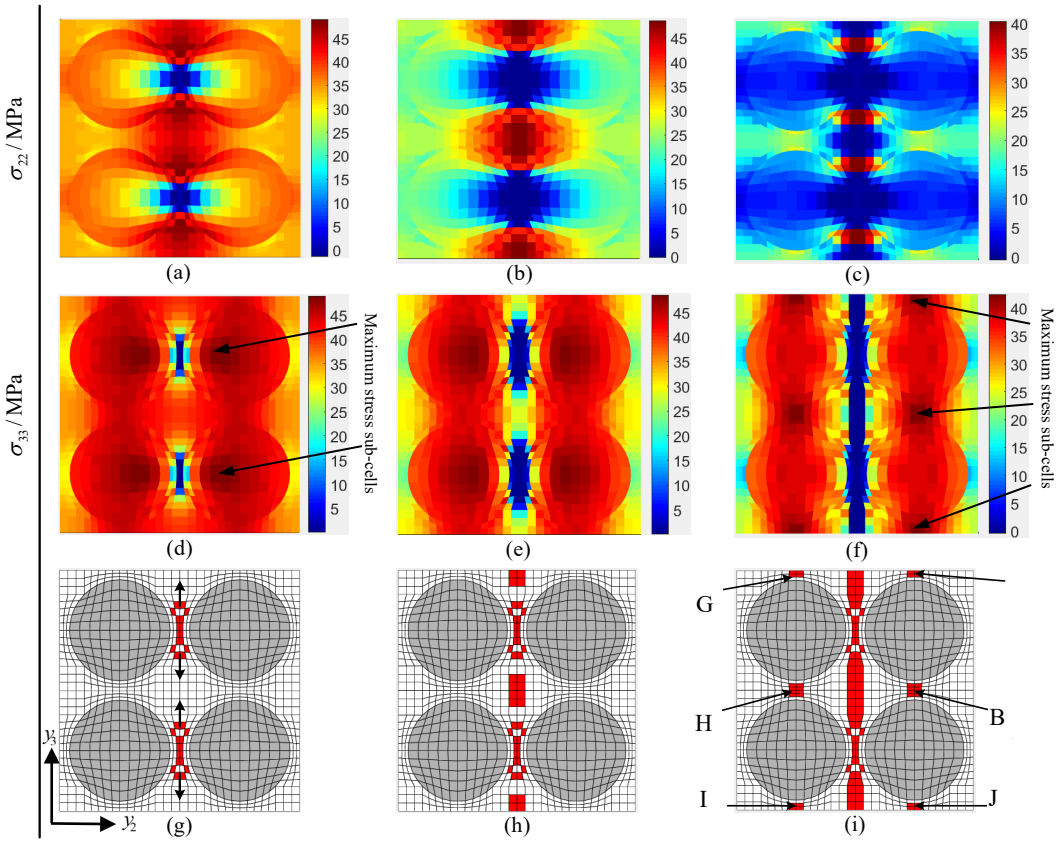

Fig. 13. Stress distributions and damage evolutions of Type-I preset damage under biaxial tensile strain

Fig. 14 shows the transverse stress-strain relation of the composites with Type-II initial damage, when tensile strains of the same magnitude are applied in the y_2- and y_3-directions simultaneously. Identical transverse stress-strain responses are found for σ_{22} and σ_{33} due to the symmetrical layout of damages "A" and "B" in relation to the loading directions (Fig 3).

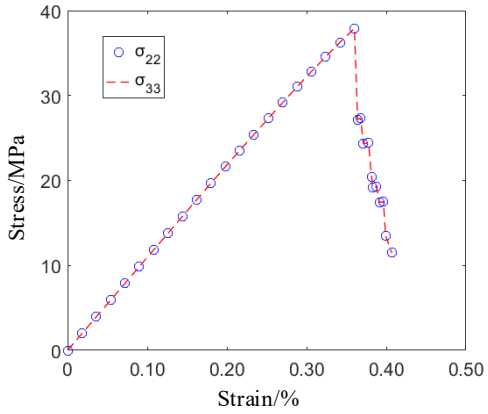

Fig. 14. Stress-strain curve of Type-II preset damage under biaxial tensile strain

Fig. 15 presents the stress contour diagram and damage evolution. The respective maximum transverse stresses σ_{22} (Fig. 15(a)) and σ_{33} (Fig. 15(d)) occur first near the initial damages "A" and "B". With an increase of the biaxial load, it is interesting to note that the maximum stress σ_{22} is always found in the matrix materials, as shown in Figs. 15(a)-(c). Figs. 15(g)-(i) show the damage evolution in the RVE. In the early loading stage, as shown in Fig 15(g), the damage evolution path is labeled by the solid lines with arrows. As the external load increases, as shown in Fig. 15(h), damage coalescence occurs first between the initial damages "A" and "B", and some new damages start to appear in the matrix located in the vicinity of "D" and "H". A further damage evolution, as well as the final failure of the RVE is shown in Fig. 15(i), which shows symmetric damage path about axis *T*-*T* due to the symmetric loading and initial damages about the same axis.

Fig. 16 indicate the stress-strain curves of the composites with Type-III preset damage subjected to the same biaxial tensile strains. The maximum transverse failure stresses along y_2-direction and y_3-direction are 36.4 MPa and 39.1 MPa, respectively. A higher stiffness property and failure strength can be found in the y_3-direction.

Fig. 17 shows the stress contour diagram and damage evolution of the composites. The maximum transverse stress σ_{22} appears first in the fiber (Figs. 17 (a)-(b)) and then moves to the matrix, as shown in Fig. 17(c). Similar stress variation are found for σ_{33}, as shown in Figs. 17(d)-(f). Although the maximum stress occurs first in the fiber, damage evolution only appears in the matrix due to their large difference in failure strengths. From Fig. 17(g), it is revealed that new damages appear first at the bottom of damage "A", and propagate in the direction of the black arrow. When the external load reaches a certain level, as shown in Fig. 17(h), it can be found that damage coalescence occurs between initial damages "A" and "B". New damages occur simultaneously at location "I". The final failures of the RVE is shown in Fig. 17(i). Some new damages can be found close to "D", and damage evolution is also found near region "I".

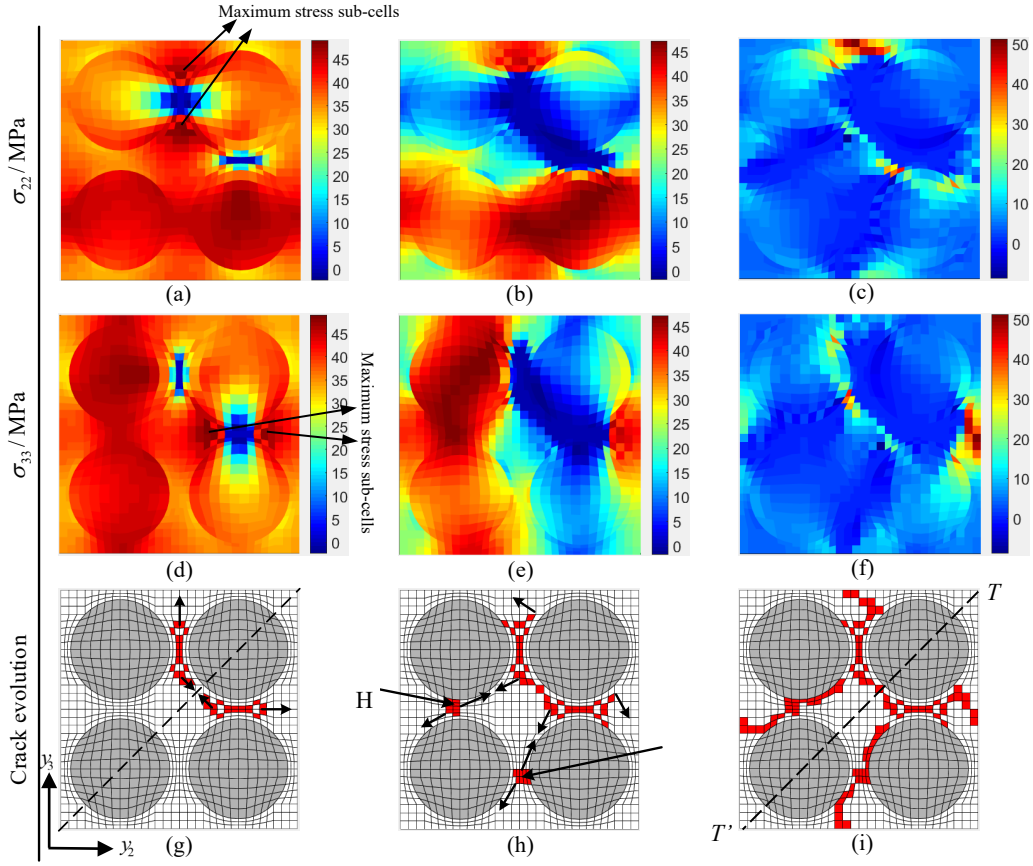

Fig. 15. Stress distributions and damage evolutions of Type-II preset damage under biaxial tensile strain

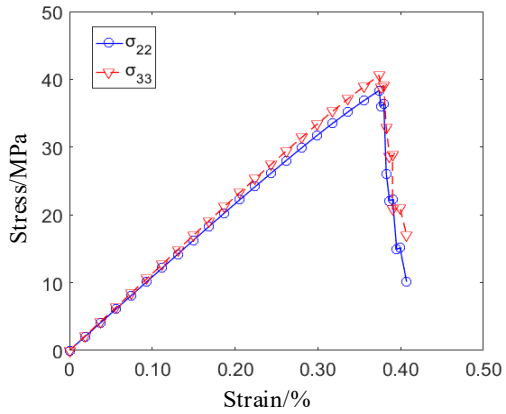

Fig. 16. Stress-strain curves of Type-III initial damage under biaxial tensile strain

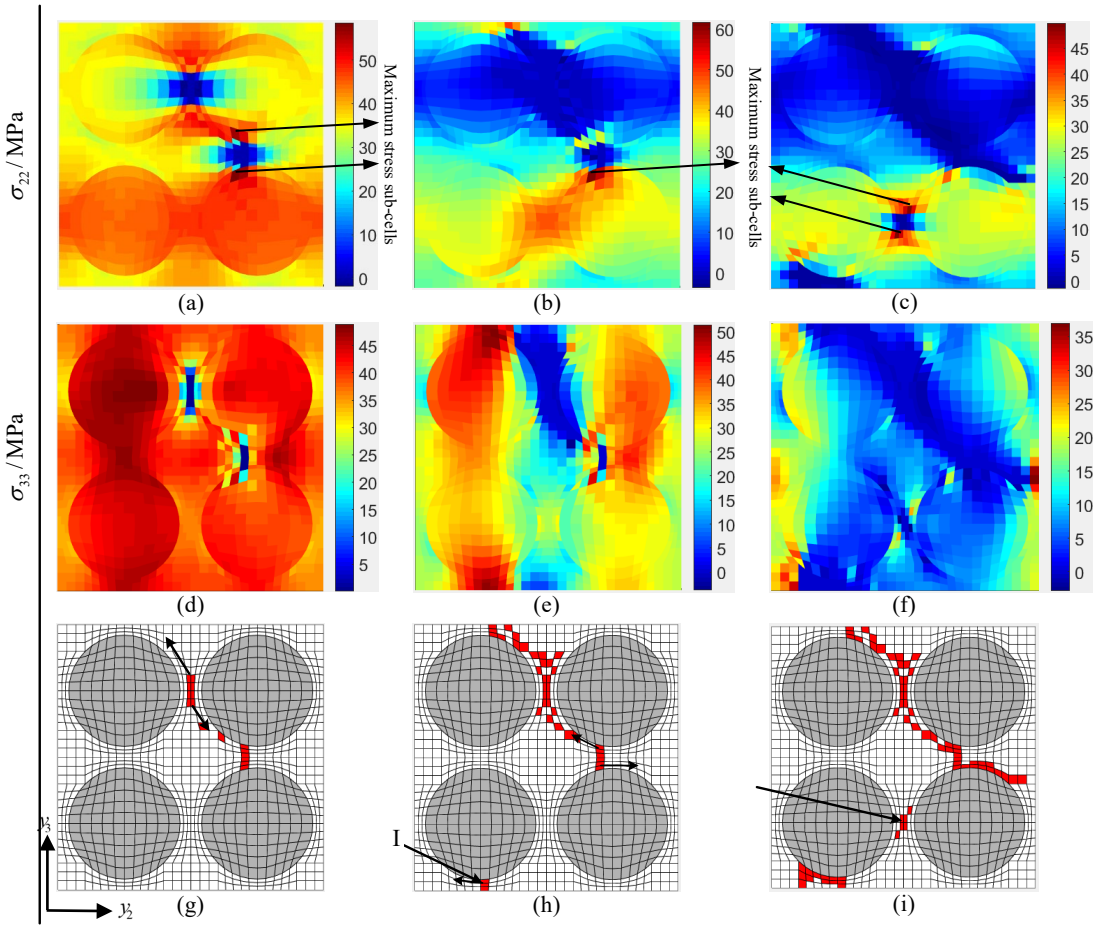

Fig. 17. Stress distributions and damage evolutions of Type-III preset damage under biaxial tensile strain

6. Conclusions

A numerical method, which is capable of modelling initial damage/voids, has been proposed in this paper to investigate microscale damage evolutions in fiber-reinforced composites subjected to uniaxial and biaxial transverse loads. Its effectiveness in predicting nonlinear deformations of the composites subjected to off-axis load were verified by comparing with experimental data. Stiffness degradation model and failure criterion were then introduced to predict failure in the RVE. The numerical results indicated that the occurrence and extension of sub-cell damages, as well as failure strength of the composites are closely dependent on initial damage mode. The conclusions are summarized below:

1) For a composite with initial damages, it was shown the proposed microscale method were accurate not only in describing stress distribution but also in predicting damage propagation at constituent material level.
2) Microscale damage evolution is closely dependent on initial defects and loading modes. It is interesting to observe that the Type-I preset damage shows identical damage evolution under tensile and compressive strains in the y_2-direction. Similar conclusions can be found for Type-III preset damage.

3) For the Type-II preset damage, the final failure of the RVE under compressive strain in the y_2-direction is attributed to damage coalescence of the two preset damages. When biaxial tensile load is considered, the final failure shows symmetric damage path about axis *T-T*.

Data availability statement

The raw/processed data required to reproduce these findings can be acquired by contacting with the corresponding authors.

CRediT authorship contribution statement

Junjie Ye: Writing-original draft, Methodology, Conceptualisation. **Yun Hong:** Writing-original draft, Methodology, Visualisation. **Lu Liu**: Validation, Data curation. **Heng Cai:** Writing-review & editing, Methodology. **Wangpeng He:** Methodology, Writing-review & editing. **Bo Huang:** Methodology, Visualisation, Software. **Mohamed Saafi**: Methodology, Conceptualisation, Supervision. **Yongkun Wang:** Validation, Data curation. **Jianqiao Ye:** Methodology, Conceptualisation, Writing-review & editing, Supervision.

Declaration of Competing Interest

The authors declare that they have no known competing financial interests or personal relationships that could have appeared to influence the work reported in this paper.

Acknowledgments

This work was supported by the National Natural Science Foundation of China, China (No. 52175112, 51675397, 51805400). The National Natural Science Foundation of Shaanxi Province, China (No. 2018JZ5005). Fundamental Research Funds for the Central Universities (No. JB210421). The 111 Project, China (No. B14042).

References:

[1] Wu R, Soutis C, Zhong S, Filippone A. A morphing aerofoil with highly controllable aerodynamic performance. Aeronaut J 2017; 121(1235): 54-72.

[2] Erik VR. Review of the design process of a representative test specimen of a structural joint of a carbon-epoxy aircraft. Polym Composite 2019; 40: E898-E911.

[3] Wu R, Sun J, Chang ZZ, Bai R, Leng JS. Elastic composite skin for a pure shear morphing wing structures. J Intel Mat Sys Str 2015; 26(3): 352-363.

[4] Keykha AH. Investigation of the behavior of deficient steel members strengthened using carbon fiber reinforced polymer under combined compressive load and torsional moment. Mech Adv Mater Struc 2020; 27(11): 894-902.

[5] Ma YQ, Wang J, Zhao YT, Wei XL, Ju LY, Chen Y. A New Vacuum Pressure Infiltration CFRP Method and Preparation Experimental Study of Composite. Polym 2020; 12(2):419.

[6] Khan, ZM, Adams DO, Anas S. The influence of multiple nested layer waviness on the compression strength of double nested wave formations in a carbon fiber composite laminate. Mech Compos Mater 2016; 51(6): 751-760.

[7] Yin JC, Zhang JH, Wang T, Zhang Y, Wang WQ. Experimental investigation on air void and compressive strength optimization of resin mineral composite for precision machine tool. Polym Composite 2018; 39(2):

457-466.

[8] Huang T, Gong YH. A multiscale analysis for predicting the elastic properties of 3D woven composites containing void defects. Compos Struct 2018; 185: 401-410.

[9] Koloor SSR, Abdullah MA, Tamin MN, Ayatollahi MR. Fatigue damage of cohesive interfaces in fiber-reinforced polymer composite laminates. Compos Sci Technol 2019; 183: 107779.

[10] Ye JJ, Wang YW, Li ZW, Saafi M, Jia F, Huang B, Ye JQ. Failure analysis of fiber-reinforced composites subjected to coupled thermo-mechanical loading. Compos Struct 2020; 235:111756.

[11] Ye JJ, Chu CC, Cai H, Hou XN, Shi BQ, Tian SH, Chen XF, Ye JQ. A multi-scale model for studying failure mechanisms of composite wind turbine blades. Compos Struct 2019; 212: 220-229.

[12] Zhang DX, Liu Y, Liu HL, Feng YQ, Guo HB, Hong ZL, Chen C, Zheng Yi. Characterisation of damage evolution in plain weave SiC/SiC composites using in situ X-ray micro-computed tomography. Compos Struct 2021; 275:114447.

[13] Cheon JH, Shin ES. Assessment of the ablation characteristics of carbon/phenolic composites using X-ray microtomography. Compos Sci Technol 2019; 182: 107740.

[14] Barbière R, Touchard F, Chocinski LA, Mellier D. Influence of moisture and drying on fatigue damage mechanisms in a woven hemp/epoxy composite: Acoustic emission and micro-CT analysis. Int J Fatigue 2020; 136: 105593.

[15] Cai H, Ye JJ, Wang YW, Saafi M, Huang B, Yang DM, Ye JQ. An effective microscale approach for determining the anisotropy of polymer composites reinforced with randomly distributed short fibers. Compos Struct 2020; 240: 112087.

[16] Fritz NK, Kopp R, Nason AK, Ni Xi, Lee J, Stein IY, Estelle Kalfon-Cohen, I. Sinclair, S. Mark Spearing, Pedro P. Camanho f,g, Brian L. Wardle New interlaminar features and void distributions in advanced aerospace-grade composites revealed via automated algorithms using micro-computed tomography. Compos Sci Technol 2020; 193: 108132.

[17] Zhang PF, Zhou W, Yin HF, Shang YJ. Progressive damage analysis of three-dimensional braided composites under flexural load by micro-CT and acoustic emission. Compos Struct 2019; 226, 111196.

[18] Cosmi F, Bernasconi A. Micro-CT investigation on fatigue damage evolution in short fibre reinforced polymers Compos Sci Technol 2013; 79(18): 70-76.

[19] Cosmi F, Ravalico C. Threshold identification for micro-tomographic damage characterisation in a short-fibre-reinforced polymer. Strain 2015; 51(3): 171-179.

[20] Ye JJ, Cai H, Liu L, Zhai Z, Victor AC, Wang YK, Wan L, Yang D.M, Chen XF, Ye JQ. Microscale intrinsic properties of hybrid unidirectional/woven composite laminates: Part Ⅰ experimental tests. Compos Struct 2021; 262: 113369.

[21] Barari B, Simacek P, Yarlagadda S, Crane RM, Advani SG. Prediction of process-induced void formation in anisotropic Fiber-reinforced autoclave composite parts. Int J Mate Form 2020; 13(1):143-158.

[22] He QH, Wang HJ, Fu KK,Ye L. 3D printed continuous CF/PA6 composites: Effect of microscopic voids on mechanical performance. Compos Sci Technol 2020, 191: 108077.

[23] Zhang A, Lu HB, Zhang DX. Research on the mechanical properties prediction of carbon/epoxy composite laminates with different void contents. Polym Composite 2016; 37(1): 14-20.

[24] Bansal Y, Pindera MJ. A second look at the higher-order theory for periodic multiphase materials. J Appl Mech-T ASME 2005; 72 (2): 177-195.

[25] Bansal Y, Pindera MJ. Finite-volume direct averaging micromechanics of heterogeneous materials with elastic-plastic phases. Int J Plasticity 2006; 22 (5): 775-825.

[26] Ye JJ, Hong Y, Cai H, Wang YK, Zhai Z, Shi BQ. A new three-dimensional parametric FVDAM for investigating the effective elastic moduli of particle-reinforced composites with interphase. Mech Adv Mater Struct 2019; 26(22):1870-1880.

[27] Chen Q, Chen XF, Yang ZB, Zhai Z, Gao JJ. Micromechanical modeling of plain woven polymer composites via 3D finite-volume homogenization. Polym Composite 2018; 39(9): 3022-3032.

[28] Khatam H, Pindera MJ. Parametric Finite-Volume Micromechanics of Periodic Materials with Elastoplastic Phases. Int J Plasticity 2009; 25: 1386-1411.

[29] Yang DH, Yang ZB, Zhai Z, Chen XF. Homogenization and localization of ratcheting behavior of composite materials and structures with the thermal residual stress effect. Mater 2019; 12(18): 3048.

[30] Chen Q, Chen XF, Zhai Z, Zhu XJ, Yang ZB. Micromechanical modeling of viscoplastic behavior of laminated polymer composites with thermal residual stress effect. J Eng Mater-T ASME 2016; 138(3): 031005.

[31] Chen Q, Tu WQ, Liu RN, Chen XF. Parametric multiphysics finite-volume theory for periodic composites with thermo-electro-elastic phases. J Intel Mat Sys Str 2018; 29(4):530-552.

[32] Xia JL, Ye JJ, Hong Y, An NL, Shi Y, Cai GG, Wang YK, He YM. Assessing effective properties of continuous carbon fiber-reinforced composites with the preset cracks. Mech Adv Mater Struct 2020; DOI: 10.1080/15376494.2020.1721622.

[33] Chen Q. Finite-Volume Micromechanics for Composite Materials with Inelastic Phases. Xi'an Jiaotong University. 2019.

[34] Wang M, Zhang PW, Fei QG. Transverse properties prediction of polymer composites at high strain rates based on unit cell model. J Aerospace Eng 2018; 31(2): 04017102.

[35] Goldberg PK, Roberts GD, Gilat A. Implementation of an associative flow rule including hydrostatic stress effects into the high strain rate deformation analysis of polymer matrix composites. J Aerospace Eng 2005; 18(1): 18-27.

[36] Mohamadi M, Heshmati, M. Failure analysis of glass-reinforced polyester mortar pipes with different cores subjected to combined loading. J Sandw Struct Mater 2019; 21(8): 2616-2653

[37] Wang ZW, Zhao JP, Zhang X. Finite element analysis of composite laminates subjected to low-velocity impact based on multiple failure criteria. Mater Res Expr 2018; 5(6): 065320.

[38] Hashin Z. Failure criteria for unidirectional fiber composites. J Applied Mech 1980; 47(2):329-334.

[39] Tsai SW, Hahn HT. Introduction to composite materials [M]. Lancaster: Technomic Publishing Co., Inc., 1980.

[40] Zhai Z. Multiscale Modeling Based on Generalized Cell of Method and its Application in Composite Health Monitoring [D]. Xi'an: Xi'an Jiaotong University, 2014.

[41] Gotsis PK, Chamis CC, Minnetyan L. Prediction of composite laminate fracture: micromechanics and progressive fracture. Compos Sci Technol 1998; 58(7): 1137-1149.

[42] Mayes JS, Hansen AC. Composite laminate failure analysis using multicontinuum theory. Compos Sci Technol 2004; 64(3-4): 379-394.

[43] Huang ZM. Abridging model prediction of the ultimate strength of composite laminates subjected to biaxial loads. Compos Sci Technol 2004; 64(3-4): 395-448.

[44] McCartney LN. Prediction of ply crack formation and failure in laminate. Compos Sci Technol 2002; 62(12-13): 1619-1631.

Appendix

$$\mathbf{T}^{-1}=\begin{bmatrix} \cos^2\theta & \sin^2\theta & 0 & 0 & 0 & -\sin 2\theta \\ \sin^2\theta & \cos^2\theta & 0 & 0 & 0 & \sin 2\theta \\ 0 & 0 & 1 & 0 & 0 & 0 \\ 0 & 0 & 0 & \cos\theta & \sin\theta & 0 \\ 0 & 0 & 0 & -\sin\theta & \cos\theta & 0 \\ \frac{1}{2}\sin 2\theta & -\frac{1}{2}\sin 2\theta & 0 & 0 & 0 & \cos 2\theta \end{bmatrix}$$